2018 IEEE/RSJ International Conference on Intelligent Robots and Systems (IROS)
Madrid, Spain, October 1-5, 2018

Multi-Limbed Robot Vertical Two Wall Climbing Based on Static Indeterminacy Modeling and Feasibility Region Analysis

Xuan Lin[1] Hari Krishnan[1] Yao Su[1] Dennis W Hong[1]

***Abstract*— This paper presents a technique to model statically indeterminate forces based on stiffness matrices for multi-limbed climbing robots. Current wall climbing robots in literature overlook statically indeterminate forces, causing an incapability to estimate climbing failure under certain circumstances. Accounting for these forces, robot deformation can be approximated, paving the way for the proposed two-wall climbing approach. During a wall climb, two failure modes, slide and over-torque, are identified to compute feasible climbing region. A hexapod robot is used to verify the proposed technique by climbing between walls with pure friction end effectors.**

I. INTRODUCTION

Climbing robots have many real world applications, such as high-rise window cleaning [1], HVAC maintenance, and vertical confined space rescue missions. Multi-limbed robots are especially adept at climbing tasks due to their added degrees of freedom from each additional limb. In general pure Coulomb friction end effectors are insufficient for maintaining robots on vertical surfaces. As a consequence numerous types of end effectors have been researched: suction cups [1], gecko feet material [2], magnets [3], microspine [4], claws [5] etc. These special end effectors cause problems, such as extra weight, power consumption, and extended end effector engagement time.

On the other hand, if a large enough normal force is applied, a robot can vertically climb with pure Coulomb friction end effectors, as seen in Fig. 1. This would eliminate aforementioned issues associated with special end effectors while introducing better dynamic properties. With two parallel walls a multi-limbed robot can generate a large enough normal force to climb by either bracing between walls or gripping the walls between its limb, *i.e. two-wall-climbing*.

For vertical climbing, the robot's full body model is essential to determine failure modes. One difficulty in modeling multi-limbed vertical climbing robots with position controlled joints is that the reaction forces are *statically indeterminate* [6], [7], *i.e.* they cannot be completely determined by the static equilibrium equations when the robot makes more than 3 contact points on the environment. To calculate the contact force completely, one needs to consider the deformation

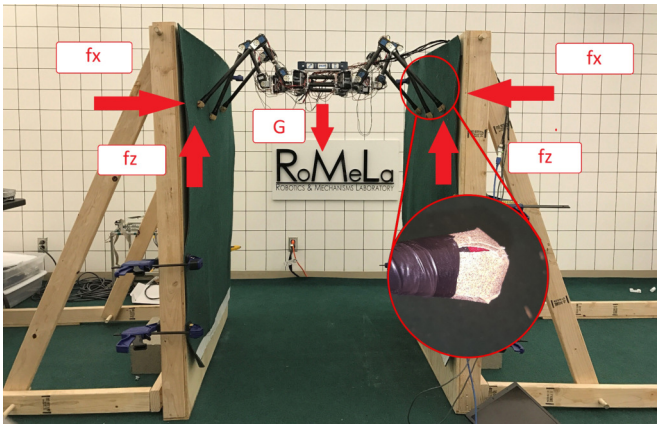

Fig. 1: Hexapod Robot climbing vertically with pure Coulomb friction end effectors (shown in the circular close-up view) by bracing between two flat walls. The width of it fully stretches out is larger than the distance between walls, creating an imposed deformation.

of the robotic system. This is especially true for *two-wall-climbing* robots, since the normal reaction forces are mostly statically indeterminate.

In wall-climbing motion planning literature, Madhani *et al.* applied standard linear programming methods to solve the linear static equilibrium equation for contact forces, leaving the *statically indeterminate* part of forces as a free parameter to optimize over [8], [9]. Bretl *et al.* investigated the feasible polyhedron for contact points and the center of mass with which the contact forces satisfy static equilibrium and friction cone constraints [10]. This line of work does not explicitly model the *static indeterminacy*. Instead these techniques show the existence of deformation by providing a solution space for the contact forces. Unfortunately, it cannot give any insight on how to physically achieve those forces, making it hard to implement on actual robots.

This can be rectified by solving for the *statically indeterminate* part of the force. To calculate this part of the force we used additional equations provided by the robot body deformation, which can be represented by its stiffness. The techniques of modeling the complete stiffness of robotic systems are studied in the field of industrial manipulators [11], [12], [13], which can be roughly divided into three categories [14]: (i) the Finite Element Analysis (FEA), (ii) the Matrix

[1]Robotics and Mechanisms Laboratory (RoMeLa), Department of Mechanical and Aerospace Engineering, University of California Los Angeles, CA 90024. maynight@ucla.edu, harikrishnan@ucla.edu, yaosu@ucla.edu, dennishong@ucla.edu

Structural Analysis (MSA), and (iii) the Virtual Joint Method (VJM). The FEA method is the most accurate but computationally intensive, making it difficult to apply online [15]. The MSA method simplifies the manipulator structure into beams, and the VJM method lumps manipulator compliance into joint compliance.

In [16] Gao et al. explore using MSA to model the limb stiffness and calculates the whole body stiffness for a multi-limbed mobile robot. MSA results in complicated expressions. A series of system identification techniques are usually conducted to retrieve accurate parameters [17]. This makes it non-trivial to implement.

This paper proposes to treat each limb of a multi-limbed robot as a manipulator and adapt the computationally effective VJM manipulator stiffness modeling technique [11] to model the stiffness of each individual limb. The sum of each limb's stiffness can sufficiently represent the whole body deformation. The required *statically indeterminate* forces are thus solved such that a multi-limbed robot would know exactly how much force it should exert in order to stay in place or climb. The proposed technique is validated by using a position controlled hexapod robot equipped with pure friction end effectors to vertically climb by bracing between walls, as shown in Fig. 1.

This paper makes the following contributions:

1) A technique that explicitly models and solves the *statically indeterminate* forces based on a multi-limbed robot's whole body stiffness.
2) A method to determine the feasibility for climbing between two walls with a pre-programmed gait.
3) A new multi-limbed robot locomotion is generated to produce large normal forces on the limbs to enable its vertical climbing with pure friction end effectors. The idea of "squeezing" the robot between walls to climb can be seen in previous robots (*e.g.* [18], [19]). But this paper presents the first example in terms of multi-limbed robot climbing gait.

The rest of the paper is organized as follows. Section II describes the multi-limbed robot platform used for the experiment in this paper and the derivation of the stiffness matrix for individual limbs and for the whole body. Section III shows the failure analysis and development of feasible climbing regions. The experiments in Section IV validate the proposed modeling and feasibility analysis by enabling the robot to climb vertically between walls. Two failure modes, slide and over-torque, are analyzed in this section as well. Section V concludes the work.

II. WHOLE BODY STIFFNESS MODELING

This section first describes the configuration of the hexapod robot platform developed. Then we derive the stiffness matrix of one of the robot's limbs. Lastly, we show how the whole body stiffness is obtained from individual limb stiffness.

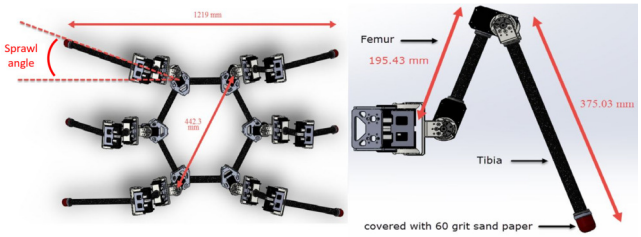

Fig. 2: Hexapod robot body dimension and position

A. Robotic Platform

The robotic platform used in this study is a hexapod design with a central body frame and 6 limb assemblies, as shown in Fig. 2. The central body frame consists of aluminum brackets interconnected with carbon fiber tubes. Each limb has 3 degrees of freedom and consists of a coxa, an upper femur, and a lower tibia assembly. The tibia and femur assemblies are made with carbon fiber tubes and are connected by a dual motor assembly.

Thirty-six MX-106 motors have been used in pairs for actuation. The stall torque for each motor pair is approximately 25.0 Nm. The robot carries its own battery, computer, and IMU. It weighs 10.3 kg. The robot's end effectors are covered by 60 grit sand paper to enhance friction. The parameters of the robot are summarized in Table I.

For multi-limbed robots like this one, most of the compliance is from the limbs as they usually have *"open"* serial structures, while the body is a *"closed"* parallel structure. Thus it is safe to assume the robot body to be rigid, and the whole body stiffness matrix can be computed with each limb's stiffness matrix.

B. VJM for a Limb Stiffness

We derive the limb's stiffness matrix in Cartesian space using VJM as done by [11]. The stiffness matrix describes the spring-like behavior of the robot's limb, assuming the shoulder is fixed with a force exerted on the end effector and each joint angle is regulated by position control. The mathematical definition of the 3D stiffness matrix is given by:

$$\underline{f} = \mathbf{K}\delta\underline{X} \tag{1}$$

where $\delta\underline{X}$ is the tiny shift in position at the end effector due to limb deformation, and $\underline{f}$ is the reaction forces

TABLE I: Robot Configuration

Parameter	Value
Degree of Freedom for Each Limb	3
Limb Coxa Length	57 [mm]
Limb Femur Length	195 [mm]
Limb Tibia Length	375 [mm]
Weight	10.3 [KG]
Motor Proportional Gain P	12
Motor Integral Gain I	0
Motor Derivative Gain D	0
Max Torque	25 [Nm]

on the end effector. Note that the definition is based on the fact that there is a fixed-end constraint on the limb shoulder, which is consistent with the mechanical design (Fig. 2).

For position controlled motors, if the motor position is regulated with only a Proportional (P) gain, the joint behaves like a torsional spring, whose spring constant is proportional to motor's P gain. For the P gain used for climbing, the robot structures are considered rigid, and the majority of the limb compliance can be lumped into the joint compliance.

Given a robot limb that has N degrees of freedom with point contact only (no torque exerted on end effector), the standard Jacobian matrix $\mathbf{J}$ is a $3\times N$ matrix. If the deformation of the robot limb is small enough, one can assume that the deformation is linear elastic. Thus the relationship between linear deflection on the end effector and the rotational deflection (similar to the rotation angle of a torsional spring) on each joint is:

$$\delta\underline{X} = \mathbf{J}\delta\underline{\theta} \tag{2}$$

where $\delta\underline{\theta}$ is the rotational deflection on each joint.

The relationship between reaction forces on the end effector and the resultant torque on each motor is:

$$\underline{\tau} = \mathbf{J}^T\underline{f} \tag{3}$$

If the P-controlled motors are modeled as torsional springs with spring coefficient k_is, the motor rotational deflection angles are:

$$\delta\theta_i = \frac{\tau_i}{k_i},\ i = 1...N \tag{4}$$

or

$$\delta\underline{\theta} = \mathbf{k}^{-1}\underline{\tau} \tag{5}$$

where:

$$\mathbf{k} = diag(k_i),\ i = 1...N \tag{6}$$

Therefore, from equation 2, plugging in equation 5 and 3, and then comparing it with equation 1, we have:

$$\mathbf{K} = (\mathbf{J}\mathbf{k}^{-1}\mathbf{J}^T)^{-1} \tag{7}$$

Note that the stiffness matrix from equation 7 will be symmetric and positive definite.

C. Whole Body Stiffness

In this subsection, the whole body stiffness matrix is assembled.

When a multi-limbed robot is climbing between 2 walls quasi-statically, each pose may be analyzed in two states. *State 1*: a human is holding the robot body while the its limbs stretch out to its commanded position with no wall contact. *State 2*: the wall is pushed in to its position and the human releases the robot's body. The difference between the commanded end effector position and the wall's position deforms the robot's limbs, and the body's center of mass has a deflection, *e.g.* the sag-down due to gravity. This causes the coordinate system attached to the body's center of mass to shift

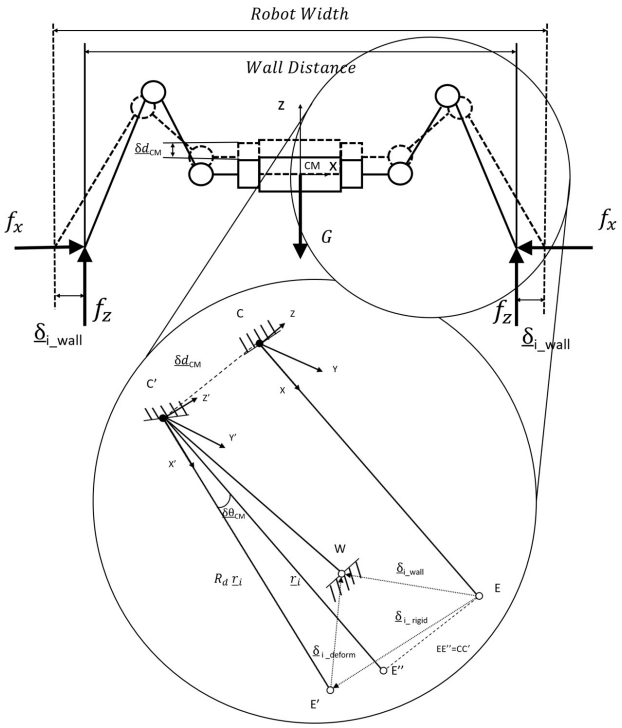

Fig. 3: Diagram of limb deformation. The upper half shows the forces and deformations of the robot bracing between walls. The dashed line shows *state 1*, while the solid line shows *state 2*. The enlarged view shows the deformation of the robot limb, where $\overrightarrow{CE}$ represents *state 1*, $\overrightarrow{C'W}$ represents *state 2*, and $\overrightarrow{C'E'}$ represents *state 3*.

and rotate by a small amount, from XYZ to $X'Y'Z'$. This physical process is depicted in Fig. 3, where $\overrightarrow{CE}$ represents *state 1*, $\overrightarrow{C'W}$ represents *state 2*.

From standard elasticity theory, the movement from *state 1* to *state 2* contains two components: one due to rigid body movement (translation and rotation) and the other due to deformation. For this reason, the wall movement does not equal to the amount of deformation for limbs. To depict the correct deformation vector, we need to get rid of the rigid body movement portion. To do so, *state 3* is introduced, which starts from *state 2* but removes the wall while keeping the body fixed, depicted by $\overrightarrow{C'E'}$. *State 3* is a transition state which releases all the deformation, so that the movement from *state 1* to *state 3* only contains rigid body motion. Let the translational part of it be from $\overrightarrow{CE}$ to $\overrightarrow{C'E''}$, and the rotational part be from $\overrightarrow{C'E''}$ to $\overrightarrow{C'E'}$. Denote body's center of mass deflection by $\underline{\delta}_{CM} = [\underline{\delta d}_{CM}, \underline{\delta\theta}_{CM}]^T$, in which $\overrightarrow{CC'} = \overrightarrow{EE''} = \underline{\delta d}_{CM}$ is the small displacement and $\underline{\delta\theta}_{CM}$ is the small rotation. The wall-imposed deflection on limb i is denoted by $\underline{\delta}_{i\_wall}$, which is a known input. From *state 1*, if we first move the limb

in parallel along $\underline{\delta d}_{CM}$ to get $\overrightarrow{C'E''}$, then rotate it to get $\overrightarrow{C'E'}$, we reach *state 3*. Then the wall deforms E' by $\underline{\delta}_{i\_deform}$ to reach W (*state 2*). Therefore $\underline{\delta}_{i\_deform}$ is the correct deformation vector for limb i, resulting in:

$$\underline{f}_i = \mathbf{K}_i \underline{\delta}_{i\_deform},\ i = 1...N \tag{8}$$

Note this equation assumes the limb is subject to a fixed-end constraint at its shoulder, which is consistent with the way stiffness matrices are defined in Section II.

From Fig. 3:

$$\underline{\delta}_{i\_deform} = \underline{\delta}_{i\_wall} - \underline{\delta}_{i\_rigid},\ i = 1...N \tag{9}$$

Wall motion $\underline{\delta}_{i\_wall}$ is a known input. To get $\underline{\delta}_{i\_deform}$, we seek an expression for $\underline{\delta}_{i\_rigid}$. Let $\mathbf{R}_d$ be the rotation matrix from frame XYZ to frame $X'Y'Z'$. Then the end effector displacement due to body rotation is $\overrightarrow{E''E'} = \mathbf{R}_d \underline{r}_i - \underline{r}_i$, where $\underline{r}_i = [x_i,\ y_i,\ z_i]^T = \overrightarrow{C'E''}$. Then we have:

$$\underline{\delta}_{i\_rigid} = \underline{\delta d}_{CM} + \mathbf{R}_d \underline{r}_i - \underline{r}_i,\ i = 1...N \tag{10}$$

When the rotation angles in $\underline{\delta\theta}_{CM}$ are infinitesimal, it can be shown [20] that $\mathbf{R}_d$ may be represented to the first order as:

$$\mathbf{R}_d = \begin{bmatrix} 1 & -\delta\theta_{CM_z} & \delta\theta_{CM_y} \\ \delta\theta_{CM_z} & 1 & -\delta\theta_{CM_x} \\ -\delta\theta_{CM_y} & \delta\theta_{CM_x} & 1 \end{bmatrix} \tag{11}$$

Where $\underline{\delta\theta}_{CM} = [\delta\theta_{CM_x}, \delta\theta_{CM_y}, \delta\theta_{CM_z}]^T$. Note this matrix is first order unitary.

Plugging equations 11 and 10 into equation 9:

$$\underline{\delta}_{i\_deform} = \underline{\delta}_{i\_wall} - [\mathbf{I}\ \mathbf{P}_i^T]\underline{\delta}_{CM},\ i = 1...N \tag{12}$$

where:

$$\mathbf{P}_i = \begin{bmatrix} 0 & -z_i & y_i \\ z_i & 0 & -x_i \\ -y_i & x_i & 0 \end{bmatrix} \tag{13}$$

And by equation 8 the reaction force on the end effector is:

$$\underline{f}_i = \mathbf{K}_i(\underline{\delta}_{i\_wall} - [\mathbf{I}\ \mathbf{P}_i^T]\underline{\delta}_{CM}),\ i = 1...N \tag{14}$$

The static equilibrium equations are:

$$\sum_{i=1}^{N} \underline{f}_i + \underline{F}_{tot} = 0 \tag{15}$$

$$\sum_{i=1}^{N} (\underline{r}_i \times \underline{f}_i) + \underline{M}_{tot} = 0 \tag{16}$$

Where $\underline{F}_{tot}$ is the total load force and $\underline{M}_{tot}$ is the total load torque.

Plug equation 14 into equation 15 and 16 to get

$$\mathbf{A}\underline{\delta}_{CM} = \begin{bmatrix} F_{tot} \\ M_{tot} \end{bmatrix} + \sum_{i=1}^{N} \begin{bmatrix} \mathbf{K}_i \underline{\delta}_{i\_wall} \\ \mathbf{P}_i \mathbf{K}_i \underline{\delta}_{i\_wall} \end{bmatrix} \tag{17}$$

Where:

$$\mathbf{A} = \sum_{i=1}^{N} \begin{bmatrix} \mathbf{K}_i & \mathbf{K}_i \mathbf{P}_i^T \\ \mathbf{P}_i \mathbf{K}_i & \mathbf{P}_i \mathbf{K}_i \mathbf{P}_i^T \end{bmatrix} \tag{18}$$

is the *whole body stiffness matrix*. Equation 17 relates the body's center of mass deflection to its loading, plus a deformation input describing the effect of the imposed wall deflection.

As a result, the complete stiffness model can be summarized by equation 7, 13, 14, 17, and 18.

Compared to previous works, especially [16] and [21], VJM, instead of MSA, is adopted to model the limb stiffness. Mobile robots tend to operate in uncertain environment and don't require high precision control. VJM method, although less accurate than MSA, models much faster, expediting its implementation. Additionally, the deformation input $\underline{\delta}_{i\_deform}$ is introduced as the difference between commanded end effector position and wall position. The robot's limb can actively change $\underline{\delta}_{i\_deform}$ by changing its commanded position to avoid failure.

III. Feasibility Analysis For Pre-programmed Climbing Gait

Based on the model developed in Section II, A method is developed to determine feasible wall-distances for the robot to climb with a pre-programmed gait. In more complicated wall profiles, we can plan the robot's wall-imposed deformation $\underline{\delta}_{i\_wall}$ to compensate for wall distance changes.

To conduct vertical wall climbing, the robot must go through a series of postures. For quasi-static climbing, one can analyze each bracing posture separately to determine failure. We identify two failure modes for climbing depending on the imposed deformation $\underline{\delta}_{i\_wall}$. If $\underline{\delta}_{i\_wall}$ is too large, *i.e.* the robot pushes into the wall too hard, it over-torques the motor, but an insufficient amount of $\underline{\delta}_{i\_wall}$ results in sliding. As it is unnecessary to analyze each frame, we pick a few key failure frames, calculate their two failure modes, and connect them into complete failure curves.

For typical multi-limbed wall climbing gaits, the robot moves its body up with all limbs attached to the wall. This is because the body usually takes majority of the robot's weight. The more limbs in contact with the wall, the safer the engagement will be when shifting the body. Therefore, the robot initially picks up a few limbs, and puts them at higher positions on wall Then it pushes its body up, and picks up other limbs and iterates. This process is exhibited in Fig. 4, where the robot takes a tripod gait (picks up three legs each time) and climbs up. The *upper diagram* in Fig. 4 demonstrates the method for analyzing feasibility for the given tripod gait. Along the continuous configurations, we pick key failure frames to be: A, B, C, D, E and F. For each key frame, the reaction force on end effector has to lie

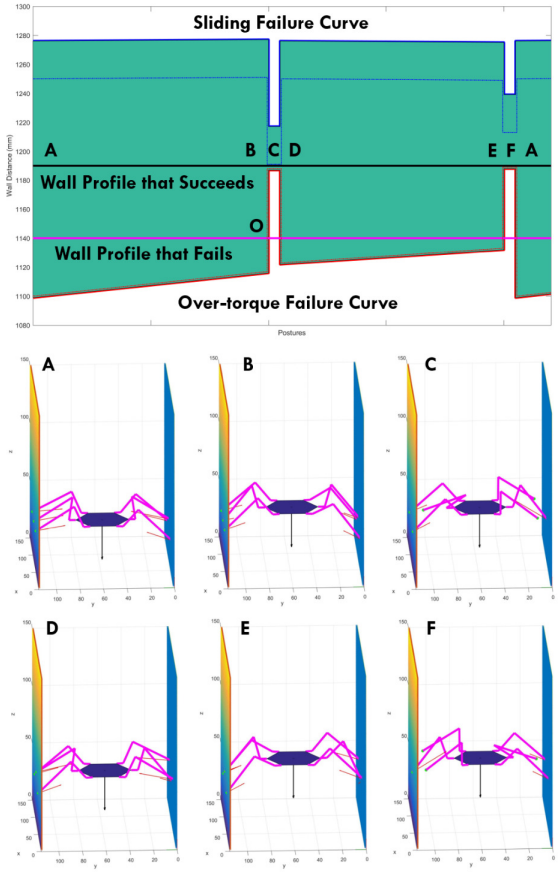

Fig. 4: Feasible region analysis for pre-programmed gait. *Upper diagram*: The robot slides when the wall distance is above the sliding failure curve, generated with coefficient of friction μ around 0.7. The motor over-torques when the wall distance is below the over-torque failure curve. The green region shows the feasible climbing wall distance. The black line shows a wall profile that the robot succeeds in climbing for the given gait. The magenta line shows a wall profile that the robot fails to climb. The dotted curves are critical failure curves. *Lower diagram*: A series of robot configurations as the robot climbs up, visualized in MATLAB. The black arrows show gravity and the red arrows show the end effector reaction force. From point A to B, the robot slowly pushes its body up. At point C, the robot picks up three limbs. At point D, the robot put three limbs back on wall. At point D to E, the robot further pushes its body up. At point F, the robot picks up the other three limbs. The letters in the *lower diagram* correspond to those in the upper.

within the friction cone for the robot not to slide. This constraint can be written as:

$$\underline{f}_i \in \underline{F}_i \tag{19}$$

where $\underline{F}_i$ represents the feasible set of contact force. The over-torque constraint can be written as:

$$\mathbf{J}^T \underline{f} < \underline{\tau}_{max} \tag{20}$$

Setting $\underline{\delta}_{i\_wall} = (RobotWidth - WallDistance)/2$, with $RobotWidth$ fixed, the over-torque/slide points are retrieved by decreasing/increasing the wall distance and then calculating the reaction force by equation 7, 13, 14, 17, and 18, until constraint 20 for over-torque, or constraint 19 for sliding, is violated. By doing so, we retrieve the key frame failure wall distance $WallDistance_{min}$ for over-torque, and $WallDistance_{max}$ for slide.

Lastly, the key frame failure wall distances are connected to generate the complete curves, as shown in the *upper diagram* in Fig. 4. The x axis doesn't have any physical meaning, it is just stacking a series of postures together. The y axis is the wall distance. From point A to point B, the robot raises its body, that the compliance of body changes continuously, since the moment arm of contact force changes. This results in a continuous change of failure curves. Since only A and B are analyzed, they are simply connected linearly. At point C, the robot picks up three legs. This causes a sharp change of failure curves, leading to the weakest failure point of the gait.

The actual wall profile must stay below the sliding failure curve for the robot not to slide and above the over-torque failure curve for the motors not to over-torque. This generates a feasible region along the posture axis as the robot climbs up, represented as the green region shown in Fig. 4. The actual wall profile can be plotted on top of it to determine feasibility. The black line shows a wall profile with a constant distance that completely stays within the feasible region, meaning the robot can successfully climb.

However, as the robot climbs up, it may encounter wall profiles that go out of the feasible region, producing a failure. This is shown in Fig. 4 *upper diagram* with the magenta curve, where the motor over-torques at point O. One way to tackle this failure is to plan $RobotWidth$ according to wall profile, instead of using a fixed $RobotWidth$. For example, the robot may decrease its $RobotWidth$ at point O. This effectively changes the wall distance that is "seen" by the robot, redirecting it into the feasible region.

Finally, if two curves cross over each other, the climbing is strictly infeasible. This can happen when the coefficient of friction is too low or when the maximum torque for the motor is too weak.

Since wall climbing is a highly dangerous task, and some factors (*e.g.* coefficient of friction) are hard to measure precisely, getting the safety factor for a given climbing motion plan is essential. Using the proposed feasibility diagram, one can also get the climbing safety factor with respect to the coefficient of friction and the motor's maximum torque. The safety factor with

respect to the coefficient of friction, S_μ, can be retrieved by gradually lowering μ from the nominal value (so the sliding failure curve will drop), until a value μ_c which makes climbing critically feasible. This defines the *sliding critical failure curve*, shown in the *upper diagram* in Fig. 4 by dotted blue curve. The sliding safety factor is $S_\mu = \mu/\mu_c$. Similarly, safety factor with respect to the motor's maximum torque, S_τ, can be retrieved by gradually lowering τ_{max} from the nominal value to get over-torque critical failure curve (shown in the *upper diagram* in Fig. 4 by dotted red curve) and critical failure torque τ_c. Thus $S_\tau = \tau_{max}/\tau_c$. In Fig. 4, $\mu_c = 0.34$, $\tau_c = 24.75$ are retrieved, thus $S_\mu = 2.06$ and $S_\tau = 1.01$ for the given tripod climbing gait.

To conclude, we generate the feasibility diagram for the *two-wall-climbing* problem, based on the model developed in Section II. The feasibility diagram can tell if climbing is feasible with a given $RobotWidth$, feasible with properly planned $RobotWidth$, or strictly infeasible. The diagram can be utilized to plan the motion for a class of different vertical climbing problems, such as climbing by grasping two vertical surfaces between its legs *e.g.* climbing up trees or lamp-posts.

It is worth mentioning that as the robot moves, the position of center of mass will change due to the change of mass distribution. For the purpose of analysis, this can be taken care of by recalculating the center of mass position for each key failure frame, and using its correct values in equation 13, 17 and 18.

IV. EXPERIMENTS

A. Verification of Stiffness Model

The general process of model verification is to regulate the imposed deformation $\underline{\delta}_{i\_wall}$ and observe the outputs: body sag-down $\underline{\delta d}_{CM}$ and reaction force $\underline{f}_i$ on the end effector. The experiment is designed to have the robot brace between two rigid walls, shown in Fig. 5, by varying the distance between walls while keeping the end effector position fixed on the wall. The end effector touching point on the wall is fixed and labeled. This controls the limb configuration the each time the experiment is conducted. One ROBOTOUS RFT60-HA01 six-axis force torque sensor is installed on the wall to measure $\underline{f}_i$ directly, shown in Fig. 5. The measurements are taken iteratively from front/back limbs. To retrieve $\underline{\delta d}_{CM}$, the joint encoder values before and after the deformation are recorded, and $\underline{\delta\theta}$ is computed. Then the limb deformation $\underline{\delta X}$ with respect to the body is calculated by equation 2, from which body shifting $\underline{\delta d}_{CM}$ can be retrieved.

On the other hand, Code is developed in MATLAB to calculate the model. To compare the calculations with experiments, virtual robot on virtual walls is setup in the code to match the experiment. The result is visualized by plotting the robot, the wall, and the reaction force contact points. The calculation outputs $\underline{\delta d}_{CM}$ and $\underline{f}_i$ are verified against experiments.

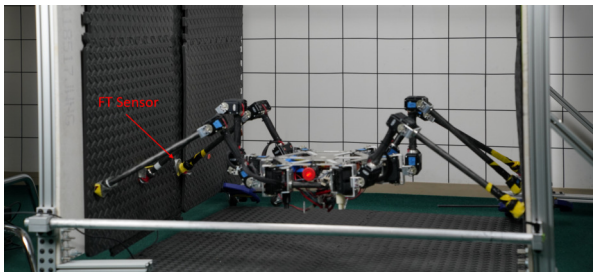

Fig. 5: Setup of Wall Bracing Test

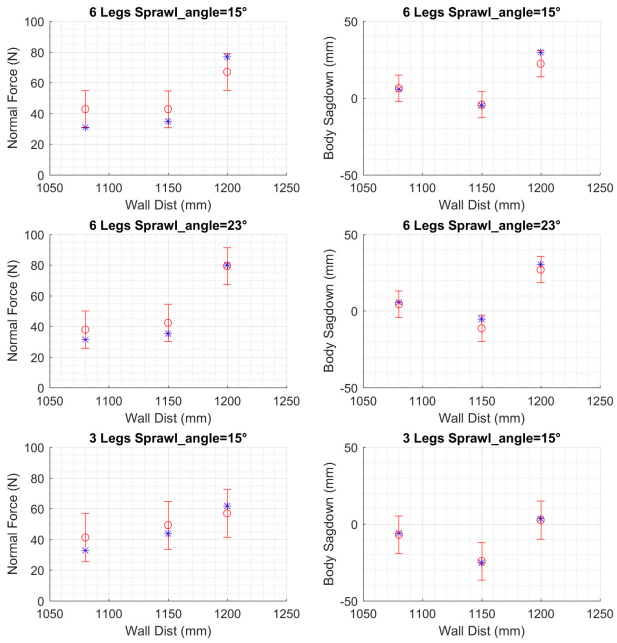

Fig. 6: Experiment results. Each set of test is done for 12 times. The blue star draws the result calculated by model. The red error bar plots the mean and the 2-sigma bound. The Wall Distances are 1080mm, 1150mm, and 1200mm, and $\underline{\delta}_{i\_wall}$ are 30mm, 20mm and 65mm respectively. The definition of sprawl angle is given in Fig. 2. In plot title "3 Legs" means 3 legs are on the wall corresponding to Fig. 4 diagram C.

Nine sets of tests with the hexapod under different configurations, different wall distances, different imposed deflection, and different number of legs on the wall, are conducted. In all tests, the robot body's initial pose is kept parallel to the ground. For each test, the wall's distance is within feasible bracing region. Experimental data F_N and δZ from the front and back limbs, the component of $\underline{f}_i$ normal to the wall and the vertical component of $\underline{\delta d}_{CM}$ along gravity direction, are plotted in Fig. 6. We only plot F_N since it is statically indeterminate, which highlights the most important feature of this model.

The joint sprint constant $k_i s$ can be found from the

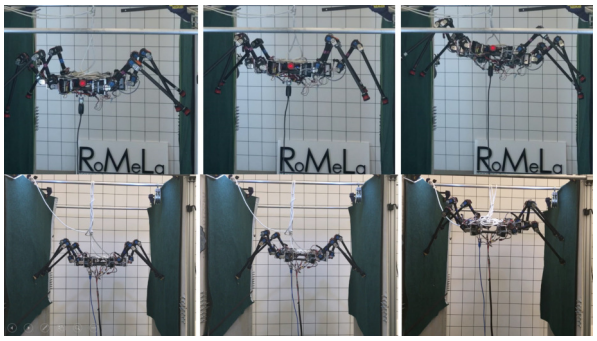

Fig. 7: Instances of climbing between walls. The upper three figures are climbing with tripod gait at t=0, t=25 and t=50 seconds, respectively. The lower three figures are climbing with ripple gait at t=0, t=10 and t=80 seconds, respectively. The wall distance is 1190mm for tripod and 1160mm for ripple.

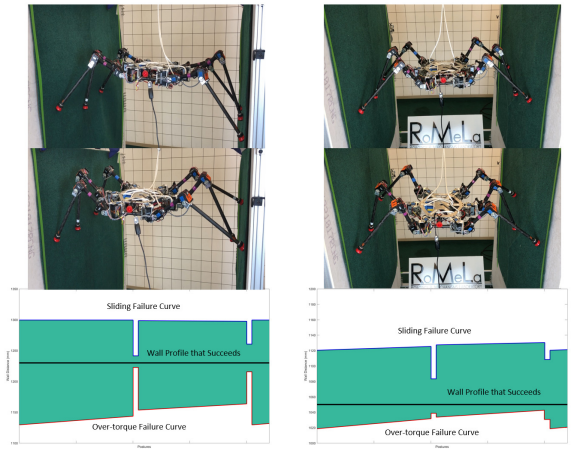

Fig. 8: Instances of climbing between walls with different wall distances. Left column: $WallDistance$=1230mm and $RobotWidth$=1300mm, picture taken at t=0 and t=20sec. Right column: $WallDistance$=1050mm and $RobotWidth$=1135mm, picture taken at t=0 and t=20sec. The black lines show the wall distance.

ROBOTIS dynamixel 106 e-manual [22] (experimentally verified). One feature of VJM is that, although only joint compliance is considered, one can account for structural compliance by lumping it onto joint compliance. Based on our work of identifying total compliance [23], we add 25% to the nominal sprint constant to produce the theoretical predictions in Fig. 6. The experimental results mostly follows the calculated results. Mobile robots are uncertain in nature, the calculated deformation is subject to errors such as non-ideal contact point geometry, motor backlash, unmodeled compliance, large deflection non-linearity, etc. However, this model captures the governing physics during its bracing posture, and predicts the correct normal force that can be used to determine failure.

Testing the total compliance for a limb requires extra setup and possibly detaching a limb. Part of the structures from our robot is thin, causing an non-negligible structural compliance. If the structure is rigid enough, VJM based methods eliminate the need to identify total compliance and can expedite the implementation process of mobile robots.

B. Verification of Climbing

1) Climbing with different wall distances: 'To verify the feasibility analysis in Section III, we conduct two more robot climbing tests with $WallDistance = 1230mm$, and $WallDistance = 1050mm$, respectively. The coefficient of friction on the wall relative to the robot's end effector is around 0.7. The climbing gait picked to conduct this set of test is the tripod gait. The robot's $RobotWidth$ is set to be 1300mm and 1135mm, and the feasibility region diagram for each $BodyWidth$ is generated based on the method developed in Section III. The instances of robot climbing and the associated feasible region diagrams are plotted in Fig. 8.

As the analysis shows, the robot will succeed in climbing on a wall in both tests. The climbing test validates this result, as we are able to make the robot climb up.

It is worthwhile to mention here that if the robot just uses an open-loop pre-programmed gait, its body tends to shift and tilt as it climbs up. This causes the climbing to be more prone to failure, because tilting causes the left and right limbs to be asymmetric, thus the limbs on one side may become much more compliant than the ones on the other side. To compensate for the tilting, each time the robot makes one step, it takes the Euler angle feedback from an IMU. On top of that, a PID controller is designed to regulate the posture. If a posture error is induced as the robot picks one limb, the robot actively changes its posture, such that when it puts the limb back on wall, it is still at the desired position. The body posture regulator considerably enhances the reliability of the two-wall climbing.

2) Climbing with different gaits: Climbing with different gaits is also studied. We pick two pre-programmed gaits: ripple (picks up one limb each time), and tripod (picks up three limbs each time). The test is conducted on the two walls with fixed distance, and the coefficient of friction is around 0.7. The feasibility diagram for ripple gait is shown in Fig. 9, for tripod is shown in Fig. 4. The fixed wall distance is depicted on the diagram. As one can tell from the diagram, in both cases the climbing is feasible. However, ripple gait has five limbs on the wall as the robot makes a step, thus the feasible region for ripple gait is much larger than feasible region for tripod gait, resulting in a larger safety factor. In fact, the safety factors are $S_\mu = 2.41$ and $S_\tau = 1.10$ for the given ripple climbing gait, which is considerably

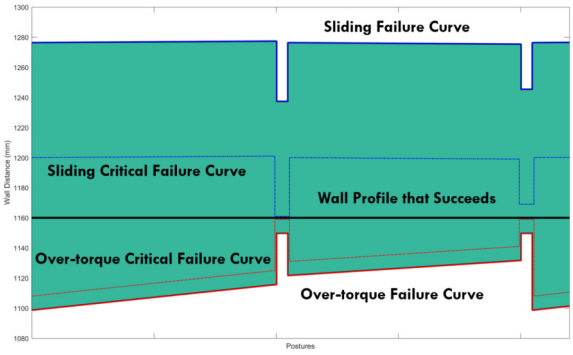

Fig. 9: Feasible climbing region for ripple gait. Only first two steps are shown, since the rest repeats. The black line shows the wall distance. The sliding critical failure curve is achieved at $\mu_c = 0.29$ and the over-torque critical failure curve is achieved at $\tau_c = 22.73$.

higher than that of the given tripod gait (provided in Section III). This is demonstrated through experiments. We are able to successfully conduct vertical climbing with both gaits, but ripple gait has a significantly lower chance to fail than the tripod gait. The results are pictured in Fig. 7 and are shown in the attached video.

V. Conclusion

This paper constructs a modeling technique based on stiffness matrix for calculating the reaction force and body deformation which explicitly takes into account the statically indeterminate force. With this unique feature, we propose a two-wall climbing approach as an extension for the multi-limbed robot locomotion method. Two failure modes: slide and over-torque, are identified. A method to compute the feasible climbing region is proposed. We verify the accuracy of modeling technique by experimentation. The computed feasible climbing region is also verified via experiments at different wall distances and different climbing gaits. The results show that the model captures majority physics for posturing the robot on wall, and the computed feasible region gives a good prediction indicating the success of a climb.

Future works may include extending the proposed two-wall climbing approach to other practical implementations such as climb up and down on trees, lamp posts, pipes, wells, and so on. This locomotion method can also be favorable for applications under low gravity environments, for instance those on Moon/Mars, where it becomes more efficient.

References

[1] Y. Guan, H. Zhu, W. Wu, X. Zhou, L. Jiang, C. Cai, L. Zhang, and H. Zhang, "A modular biped wall-climbing robot with high mobility and manipulating function," *IEEE/ASME transactions on mechatronics*, vol. 18, no. 6, pp. 1787–1798, 2013.

[2] S. Kim, M. Spenko, S. Trujillo, B. Heyneman, D. Santos, and M. R. Cutkosky, "Smooth vertical surface climbing with directional adhesion," *IEEE Transactions on robotics*, vol. 24, no. 1, pp. 65–74, 2008.

[3] S. Hirose and H. Tsutsumitake, "Disk rover: A wall-climbing robot using permanent," in *International Conference on Intelligent Robots and Systems (IROS)*, vol. 3, pp. 2074–2079, IEEE, 1992.

[4] A. Parness, N. Abcouwer, C. Fuller, N. Wiltsie, J. Nash, and B. Kennedy, "Lemur 3: A limbed climbing robot for extreme terrain mobility in space," in *International Conference on Robotics and Automation (ICRA)*, pp. 5467–5473, IEEE, 2017.

[5] J. Clark, D. Goldman, P.-C. Lin, G. Lynch, T. Chen, H. Komsuoglu, R. J. Full, and D. E. Koditschek, "Design of a bio-inspired dynamical vertical climbing robot.," in *Robotics: Science and Systems (RSS)*, 2007.

[6] V. Kumar and K. Waldron, "Force distribution in walking vehicles," *Journal of Mechanical Design*, vol. 112, no. 1, pp. 90–99, 1990.

[7] D. W. Hong and R. J. Cipra, "Visualization of the contact force solution space for multi-limbed robots," *Journal of Mechanical Design*, vol. 128, no. 1, pp. 295–302, 2006.

[8] A. Madhani and S. Dubowsky, "Motion planning of mobile multi-limb robotic systems subject to force and friction constraints," in *International Conference on Robotics and Automation (ICRA)*, pp. 233–239, IEEE, 1992.

[9] A. Madhani and S. Dubowsky, "The force workspace: A tool for the design and motion planning of multi-limb robotic systems," *Journal of Mechanical Design*, vol. 119, no. 2, pp. 218–224, 1997.

[10] T. Bretl, "Motion planning of multi-limbed robots subject to equilibrium constraints: The free-climbing robot problem," *The International Journal of Robotics Research*, vol. 25, no. 4, pp. 317–342, 2006.

[11] J. K. Salisbury, "Active stiffness control of a manipulator in cartesian coordinates," in *Decision and Control including the Symposium on Adaptive Processes, 1980 19th IEEE Conference on*, vol. 19, pp. 95–100, IEEE, 1980.

[12] A. Klimchik, A. Pashkevich, and D. Chablat, "Cad-based approach for identification of elasto-static parameters of robotic manipulators," *Finite Elements in Analysis and Design*, vol. 75, pp. 19–30, 2013.

[13] S. Marie, E. Courteille, and P. Maurine, "Elasto-geometrical modeling and calibration of robot manipulators: Application to machining and forming applications," *Mechanism and Machine Theory*, vol. 69, pp. 13–43, 2013.

[14] A. Pashkevich, A. Klimchik, and D. Chablat, "Enhanced stiffness modeling of manipulators with passive joints," *Mechanism and machine theory*, vol. 46, no. 5, pp. 662–679, 2011.

[15] G. Piras, W. Cleghorn, and J. Mills, "Dynamic finite-element analysis of a planar high-speed, high-precision parallel manipulator with flexible links," *Mechanism and machine theory*, vol. 40, no. 7, pp. 849–862, 2005.

[16] X. Gao and S.-M. Song, "A stiffness matrix method for foot force distribution of walking vehicles," *IEEE transactions on systems, man, and cybernetics*, vol. 22, no. 5, pp. 1131–1138, 1992.

[17] G. Alici and B. Shirinzadeh, "Enhanced stiffness modeling, identification and characterization for robot manipulators," *IEEE transactions on robotics*, vol. 21, no. 4, pp. 554–564, 2005.

[18] S.-g. Roh and H. R. Choi, "Differential-drive in-pipe robot for moving inside urban gas pipelines," *IEEE transactions on robotics*, vol. 21, no. 1, pp. 1–17, 2005.

[19] J. M. Friesen, P. Glick, M. Fanton, P. Manovi, A. Xydes, T. Bewley, and V. Sunspiral, "The second generation prototype of a duct climbing tensegrity robot, ducttv2," in *Robotics and Automation (ICRA), 2016 IEEE International Conference on*, pp. 2123–2128, IEEE, 2016.

[20] T. Bretl and S. Lall, "A fast and adaptive test of static equilibrium for legged robots," in *Robotics and Automation, 2006. ICRA 2006. Proceedings 2006 IEEE International Conference on*, pp. 1109–1116, IEEE, 2006.

[21] X. Gao, S.-M. Song, and C. Q. Zheng, "A generalized stiffness matrix method for force distribution of robotic systems with indeterminancy," *Journal of Mechanical Design*, vol. 115, no. 3, pp. 585–591, 1993.

[22] "Robotis e-manual v1.31.30: Mx-106t / mx-106r."

[23] X. Lin and D. W. Hong, "Convexity of stiffness matrix eigenvalues for a position controlled limb of mobile climbing robots," in *Humanoid Robots (Humanoids), 2016 IEEE-RAS 16th International Conference on*, pp. 1161–1166, IEEE, 2016.